Letters

Impact and Mitigation of High-Frequency Side-Channel Noise Intrusion on the Low-Frequency Performance of an Inverter

Nanditha Gajanur, *Student Member, IEEE*, Mateo D. Roig Greidanus, *Student Member, IEEE*, Sudip Kumar Mazumder, *Fellow, IEEE*, and Mohammad Ali Abbaszada, *Student Member, IEEE*

***Abstract*—This letter investigates and demonstrates, experimentally, the impact of a high-frequency side-channel noise intrusion (SNI) on an output-voltage feedback signal on the low-frequency performance of a three-phase inverter. The high-frequency SNI originates at frequencies that are in the vicinity of the sampling frequency (and its multiples) of the inverter. The resultant noise-injected output-voltage feedback signal is fed to a controlling digital signal processor that experiences feedback aliasing effect due sub-Nyquist-frequency sampling. The impacts of these aliasing effects are observed at sub- or super-60-Hz frequencies of the output voltages of the inverter. Subsequently, a Kalman-filter-estimation-based control approach is pursued to mitigate this detrimental effect and its efficacy demonstrated experimentally.**

***Index Terms*—Harmonics, inverter, Kalman filtering, model-based control, noise injection.**

I. Introduction

THE increased coupling between embedded processors and sensors exposes the vulnerabilities of closed-loop control systems to potential noise-injected attacks [1], [2]. The intruders gather relevant information regarding the operation of the system and sensor to induce noninvasive sensor spoofing [3], [4]. High power antennas and amplifiers or thin electromagnetic actuators placed close to the sensors can be used to achieve intentional electromagnetic attack (IMEA) against embedded system components, as demonstrated in [5] and [6]. Model-based control of inverters, which require accurate sensor feedback and estimation [7], are especially susceptible to such side-channel noise attacks that can contaminate or corrupt the feedback signals thereby degrading or destabilizing the control system, which may require involved attack identification schemes [8] and mitigation [9], [10].

This work, given this backdrop, studies experimentally the effect of a specific type of intrusion, which contaminates the output-voltage signal of an inverter and investigates its impact on the performance degradation of the inverter leading to a simple solution that mitigates the problem. Unlike conventional sensor-attack scenarios [11], [12], in this work, we consider the side-channel noise intrusion (SNI) at the gateway to the digital signal processor (DSP) controller. We investigate, in Section II, using phase-plane and frequency-domain analyses, the impact of the proximity of the SNI noise frequency to the sampling frequency of the inverter. The effect reported is not due to false data injection but due to aliasing effect attributed to the frequency of the noise. Subsequently, based on this dynamical understanding, we outline in Section III, a SNI mitigation scheme that leverages Kalman-filter-based estimation and event detection, to normalize the performance of the inverter. Finally, in Section IV, we concludes this article.

II. Impact of Noise Injection on the Inverter Dynamics

We consider here an SNI based on malicious noise injection to feedback signals. Kune *et al.* [13] explore such baseband noise-injection methods. These techniques inject noise within the sensor bandwidth and are thus effective against sensors equipped with filters. However, the intruder may introduce high-frequency additive noise in the circuit at the point *beyond the filter* at the gateway to the controller. The following sections outline the theory of such an SNI and analysis of its influence on the inverter behavior.

A. Effect of Noise Frequency for a Given Sampling Rate (T_s)

Consider, as illustrated in Fig. 1, one phase of the inverter-output-voltage measurement, represented as $v_a(t) = V_m \cdot \sin(\omega_m t)$ (with $\omega_m = 2\pi f_m$), which is corrupted by a sinusoidal noise signal represented as $n_a\ (t) = N_l\ \cdot \sin(\omega_l t)$ (with $\omega_l =\ 2\pi f_l$). This yields a combined continuous signal $s_a\ (t) = v_a\ (t) + n_a(t)$, which is fed to the analog-to-digital converter (ADC) that is part of a monolithic DSP controller.

Now, the impulse sampling of $s_a(t)$ yields the following:

$$s_\delta\ (t) = s_a\ (t)\ .p\ (t) \tag{1}$$

Manuscript received March 18, 2022; revised April 19, 2022; accepted April 24, 2022. Date of publication April 27, 2022; date of current version June 24, 2022. This work was supported in part by the U.S. Department of Energy's Office of Energy Efficiency and Renewable Energy under Solar Energy Technology Office Award DE-EE0009026 and Award DE-EE0009349. *(Nanditha Gajanur, Mateo D. Roig Greidanus, and Sudip K. Mazumder contributed equally to this work.) (Corresponding author: Sudip Kumar Mazumder.)*

The authors are with the Department of Electrical and Computer Engineering, University of Illinois at Chicago, Chicago, IL 60607 USA (e-mail: ngajan2@uic.edu; mgreid2@uic.edu; mazumder@uic.edu; mabbas21@uic.edu).

Color versions of one or more figures in this article are available at https://doi.org/10.1109/TPEL.2022.3170885.

Digital Object Identifier 10.1109/TPEL.2022.3170885

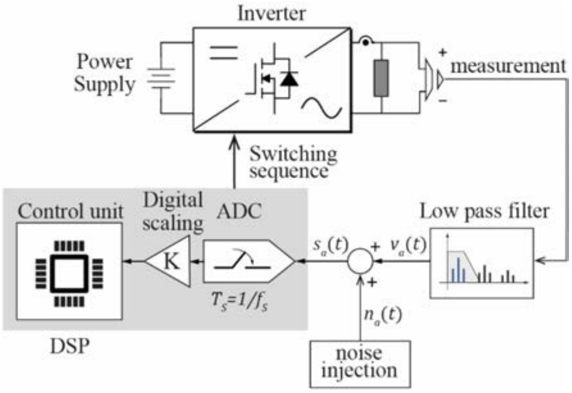

Fig. 1. Illustration of the noise-injection mechanism in the control loop. The elaborated control scheme is outlined in Section III.

where $p(t)$ is an infinite summation of impulses given by

$$p\ (t) = \sum_{n=-\infty}^{\infty} \delta\left(t - nT_s\right)\ . \tag{2}$$

In the frequency domain, (1) is captured using the following convolution (∗) for arbitrary angular frequency ω:

$$S_\delta\ (\omega) = \frac{1}{2\pi}\, S_a\left(\omega\right) * P\left(\omega\right). \tag{3}$$

In (3), $S_a(\omega)$ is the frequency-domain representation of $s_a(t)$ and $P(\omega)$ is the frequency-domain representation of $p(t)$ given by the following expression:

$$P\left(\omega\right) = \frac{2\pi}{T_s} \sum_{k\ =\ -\infty}^{\infty} \delta\left(\omega - k\omega_s\right) \tag{4}$$

where $\omega_s = \frac{2\pi}{T_s}$. Using (3) and (4), one obtains the following:

$$S_\delta\ (\omega) = f_s \sum_{k\ =\ -\infty}^{\infty} S_a\left(\omega - k\omega_s\right) \tag{5}$$

which is rewritten, given $s_a\ (t) = v_a\ (t) + n_a(t)$, as follows:

$$S_\delta\left(\omega\right) = f_s\left(\sum_{k=-\infty}^{\infty}\Big(V_a\left(\omega_m - k\omega_s\right) + N_a\left(\omega_l - k\omega_s\right)\Big)\right) \tag{6}$$

where $V_a(\omega)$ and $N_a(\omega)$ are the frequency-domain representations of sampled $v_a(t)$ and $n_a(t)$, respectively.

Now, for the inverter at hand given that $\omega_m = \ 2\pi(60)$ rad/s and $\omega_s = \ 2\pi(42k)$ rad/s (matching the switching angular frequency of the inverter), it can be concluded that the first term in (6) yields frequency components of $V_a(\omega_m - k\omega_s)$ for varying k that are wide apart in the frequency spectrum and, hence, the fundamental component can be easily filtered out by the DSP. However, in (6), the noise-frequency term $N_a(\omega_l - k\omega_s)$ yields a component at ω_m if $\omega_l = \omega_m\ + k\omega_s$. This aliased signal is problematic, as demonstrated in Section II-B since it exactly matches the desired angular frequency of the inverter and cannot be filtered out. On a related note, if $\omega_l = \ k\omega_s$, then, $N_a(\omega_l - k\omega_s)$ yields a dc component, which is problematic as well. An ultimate point is that the impact of such detrimental aliasing effects due to the noise on the low-frequency inverter dynamics can be achieved at discrete values of ω_l even at very high frequency of injections, which are relatively easier to achieve even radiatively.

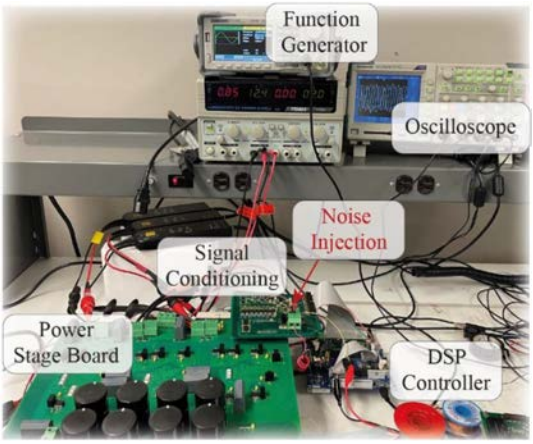

Fig. 2. Hardware setup to explore the impact of high-frequency SNI on the low-frequency performance of an ANPCI and devise mitigation.

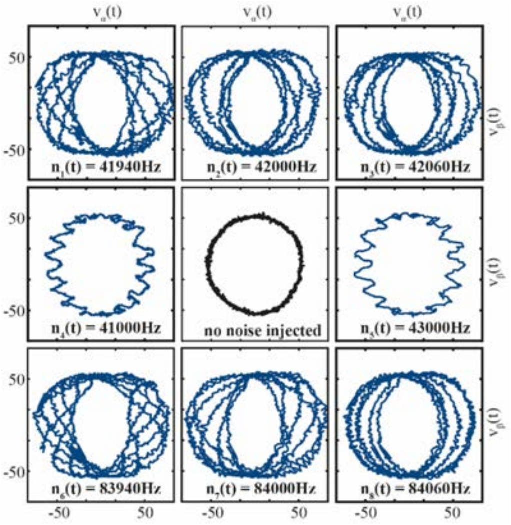

Fig. 3. Effects of the frequencies of SNIs on the inverter output voltages.

B. Experimental Analysis of SNI

To experimentally study the impact of SNI, a 3-kW standalone three-phase active-neutral-point-clamped inverter (ANPCI) hardware, as shown in Fig. 2, is used, with following additional parameters: fundamental frequency (f_m) of 60 Hz, switching frequency of 42 kHz, sampling frequency (f_s) of 42 kHz, nominal dc voltage of 200 V, nominal output voltage of 53 V rms, filter inductance (L_f) and capacitance (C_f) of 0.5 mH and 3.9 μF, respectively, and split capacitors of value of 2.04 mF. Following Fig. 1, a low-amplitude sinusoidal noise is additively injected to the phase-A output voltage of the inverter and the resultant signal is fed to an input pin of an ADC that is an integral part of a TMS320F28335 DSP controller.

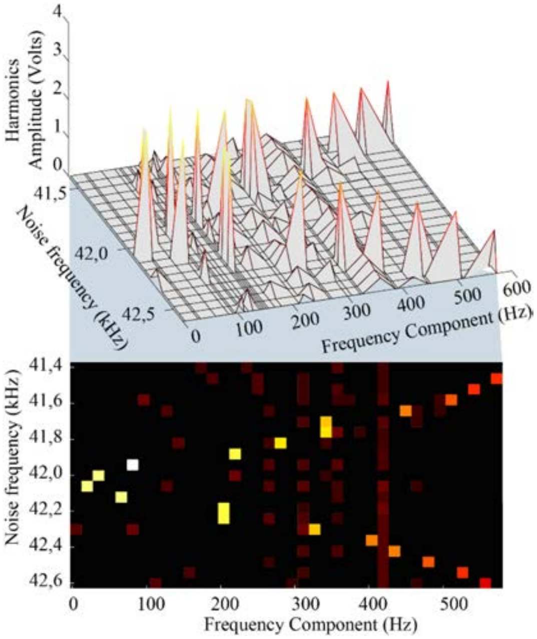

Fig. 4. Effect of SNI noise frequencies on harmonic frequency components (and respective amplitudes) of the inverter output voltage.

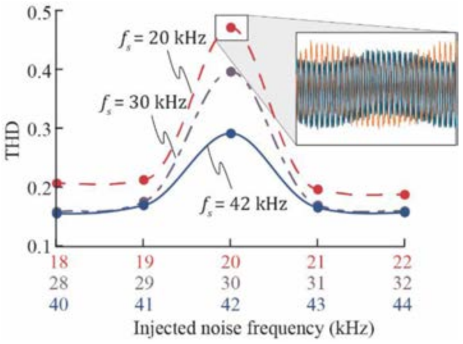

Fig. 5. Effect of SNI noise frequencies on the THD of the inverter output voltage for different sampling frequencies when the amplitude of $n_a(t)$ is set at 20% of $v_a(t)$. For a comparison, the THD is around 4% without noise.

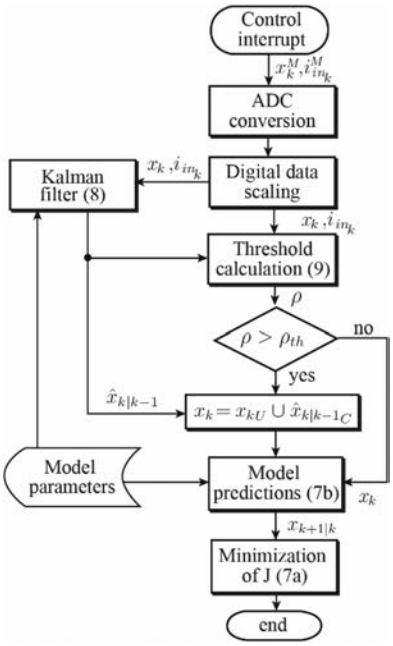

Fig. 6. Control strategy for mitigating impact of SNI, where x_k^M represents the measured states, x_{kU} and $\hat{x}_{k|k-1_C}$ represent the subsets of uncontaminated and contaminated states of x_k and $\hat{x}_k$, respectively.

Fig. 3 captures experimentally the impact of SNI on the inverter-output-voltage dynamics captured in the alpha–beta ($\alpha\beta$) stationary frame with the baseline output-voltage signal, without noise, shown in the middle. Following Section II-A, and as shown in Fig. 3, when the SNI noise frequency is so set such that the absolute deviation between it and the sampling frequency (or its integer multiple) is the inverter fundamental output frequency or null, then, the stability of the fundamental (60 Hz) periodic orbit of the inverter is compromised. A parametric analysis in Fig. 4 shows that for such SNI conditions, *sub-60-Hz frequency components* are evident in the inverter output voltage, which is consistent with the phase-plane plots shown in Fig. 3. For SNIs, where the deviation in frequencies is larger (e.g., plots corresponding to 41.5/42.5 kHz), the 60-Hz orbital stability seems ensured with the aliasing frequency component riding on it resulting in super-60-Hz harmonics. Similar effects are observed under different sampling and switching frequencies. At lower sampling frequencies, subharmonic effects make an even pronounced contribution to the total harmonic distortion (THD) of the system, as shown in Fig. 5.

III. Approach to Mitigating the Impact of the SNI

A. Control Strategy

The inverter control scheme has two operating modes, as shown in Fig. 6. In the nominal mode of operation, the ANPCI is controlled using the model-based optimal controller described by (7), which generates the time evolution of the switching states (i.e., switching sequences) for the inverter.

Minimize the cost function J subject to

$$J = \sigma_1 \left(v_\alpha^{\text{ref}} - v_{\alpha k+1}\right)^2 + \sigma_2 \left(v_\beta^{\text{ref}} - v_{\beta\, k+1}\right)^2 + \sigma_3 \left(v_{NP\, k+1}\right)^2 \tag{7a}$$

$$x_{k+1} = \Phi_j \left(t_1, t_2, \ldots, t_N\right) x_k + \Gamma_j \left(t_1, t_2, \ldots, t_N\right) \left[i_{\text{in}\, k} \quad i_{\text{out}\, k}\right]^T \tag{7b}$$

$$\sum_{i=1}^{N} t_i = T_s \tag{7c}$$

where

$\sigma_1,\ \sigma_2,\ \sigma_3 \triangleq$ normalized weighting factors;
$(v_\alpha v_\beta)^T = T_C (v_a v_b v_c)^T$ ($\alpha\beta$ components of inverter output voltages $\vec{v}_{abc}$);
$(v_\alpha^{ref}\ v_\beta^{ref})^T =$ Output voltages reference ($\alpha\beta$ frame);
$T_C \triangleq (\frac{2}{3},\ -\frac{1}{3}, -\frac{1}{3}; 0,\ \frac{1}{\sqrt{3}}, -\frac{1}{\sqrt{3}})$ (Clarke's transformation);
$v_{NP},\ i_{\text{out}},\ i_{\text{in}} \triangleq$ Defined in (A3) and (A4), inverter input current;
$x_k \triangleq$ Inverter states defined in Appendix A;
$\Phi_j(\cdot),\ \Gamma_j(\cdot) \triangleq$ Functionals defined in (A1) and (A2);

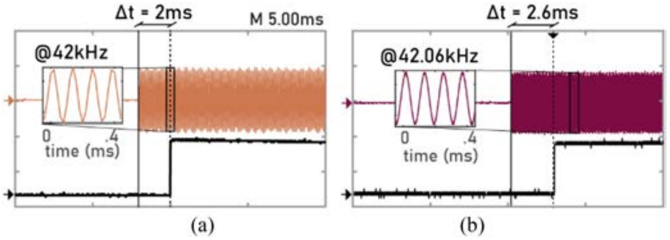

Fig. 7. Experimental result showing the response time of the mitigation scheme when $v_a(t)$ is contaminated with $n_a(t)$ at frequencies of (a) 42 kHz and (b) 42.06 kHz, respectively. In (a) and (b), the top trace shows $n_a(t)$ (with a zoom sectional view) and the bottom trace shows the time it takes for the mitigation to initiate after the onset of noise.

$t_i \triangleq$ Timings of the inverter switching states.

Now, during nominal operation if measurement of the inverter state(s) is contaminated due to SNI, then, the inverter control is compromised. To mitigate the effects of the contaminated feedback state(s), a noise-rejection-estimation-based technique is employed [11], [14]. Kalman filter [15], as captured in the generalized structure (8), is used to estimate all the contaminated state(s) of the inverter

$$\hat{x}_{k+1|k} = \Phi_j\,\hat{x}_{k|k-1} + \Gamma_j\left[i_{\text{in}k}\;i_{\text{out}k}\right]^T + L\,\left(y_k - C\hat{x}_{k|k-1}\right). \tag{8}$$

In (8), $L = (\Phi_j PC^T)\,(CPC^T + R)^{-1}$, *P* is a positive definite matrix that minimizes the steady-state covariance between x_k and $\hat{x}_{k+1|k}$, $y_k = C \cdot x_k$, where C is an identity matrix, whose dimension depends on the number of measured inverter states that are contaminated, and *R* represents the covariance of the measurement noise. To mitigate the impact of the SNI in this control mode, and as illustrated in Fig. 6, the estimate of the contaminated measurement augments the uncontaminated measured states to build (7b) and execute the optimal control. Mitigation control is triggered by comparing ρ in (9), which is evaluated over a *M*-sample window length and accumulates the error between the estimated and the measured variables

$$\rho = \frac{\sum_{j=1:M}\left(\hat{x}_{(k|k-1)_j} - x_{kj}\right)^2}{\sum_{j=1:M}\hat{x}_{(k|k-1)j}{}^2}. \tag{9}$$

with a threshold (ρ_{th}). For this illustrative work, ρ_{th} is so chosen such that noise frequencies that yield sub-60-Hz effects are detected relatively quickly with finite M. As such, for a given ρ_{th}, noise frequencies that yield sub-60-Hz effects on the output waveform yield faster detection while noise frequencies that yield super-60-Hz effects take longer detection time. One way to reduce detection time without enhancing false detections is to adaptively change ρ_{th} for a finite M or vice-versa, which involves detailed mathematical analysis (e.g., [16]–[18]) using probability theory and is a subject of a future work.

B. Experimental Validation

To validate the mitigation approach outlined in Section III-A, the test setup in Fig. 2 is used to run different scenarios when $v_a(t)$ is corrupted using $n_a(t)$. Fig. 7 demonstrates the efficacy of the mitigation and the detection schemes when $n_a(t)$ contaminates the feedback signal ($v_a(t)$) at 42- and 42.06-kHz noise frequencies. For noise frequencies that yield super-60-Hz effects, the detection time was found to be at least twice as long. This could once the mitigation strategy is triggered after the detection of the noise (as indicated by the binary jump in the event-detection signal), the performance of the inverter (as indicated by the output voltages in the $\alpha\beta$ phase plane) shows a tangible improvement, as evident in Fig. 8.

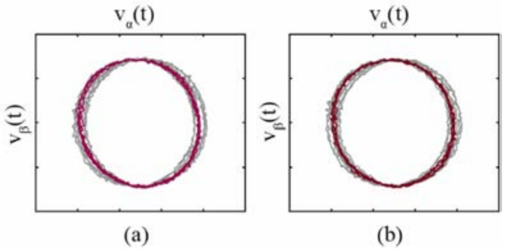

Fig. 8. Output voltages of the inverter in $\alpha\beta$ stationary frames with frequency of $n_a(t)$ being (a) 42 kHz and (b) 42.06 kHz, respectively, and the amplitude of $n_a(t)$ is set at 5% of $v_a(t)$. In (a) and (b), the background grey and foreground red traces show the responses of the inverter in the presence of the noise but without and with mitigation, respectively. In (a) and (b), the horizontal and vertical divisions stand for 25 V.

IV. Conclusion

This letter demonstrates how SNI of an inverter-output-voltage measurement signal even at high frequency impacts detrimentally the low-frequency dynamics of the inverter. What is observed is that these effects have different manifestations depending on the SNI noise frequency relative to the sampling frequency of the discrete controller. When the absolute deviation of the noise and the sampling (or integer multiples of sampling) frequencies match or is within the bound of the fundamental output frequency of the inverter, sub-60-Hz harmonic components are evident on the output voltage signals. However, when the deviation is larger, super-60-Hz harmonics are noticeable. Should such an inverter be connected to a 60-Hz grid, the injection of sub-60-Hz harmonic could be a problem and the inverter may have to be disconnected. What is further interesting is that such a scenario can be created even at progressively higher set of SNI noise frequencies, which may be practically achievable using even radiative noise injection.

After the analysis of the impact of the SNI, a simple mitigation approach is outlined. The mitigation approach initially detects the onset of the noise using an event-triggered approach where the event is generated when the deviation between the measured value of a contaminated signal and its estimate obtained using a Kalman filter exceeds a threshold. Subsequently, the estimated signal is used along with other uncontaminated measured feedback to execute a model-based optimal controller for the inverter, which is also used for noise-free conditions but with only measured feedbacks. A 3-kW experimental inverter hardware is developed that demonstrates the impact of the SNI and the efficacy of its mitigation.

APPENDIX A: MODEL SUPPORT FOR (7B)

Model of the inverter following Feng *et al.* [19] is captured by (7b)

$$x_{k+1} = \Phi_j\left(t_1, t_2, \ldots, t_N\right) x_k + \Gamma_j\left(t_1, t_2, \ldots, t_N\right)\left[i_{\text{in}\,k}\ i_{\text{out}\,k}\right]^T \tag{7b}$$

where t_i represents the duration of the ith of the N subintervals of a switching cycle that has a period of T_s, j represents the operating sector of the inverter determined using the $\alpha\beta$ references, and

$$\Phi_j\ \left(t_1, t_2, \ldots, t_N\right) = \prod_{i=1}^{N} e^{A_{(N-i+1)j}\left(t_{N-i+1}\right)} \tag{A1}$$

$$\begin{aligned}\Gamma_j\ \left(t_1, t_2, \ldots, t_N\right) &= \left(\prod_{i\neq 1}^{N} e^{A_{(N-i+1)j}(\tau)}\right)\int_0^{t_1} e^{A_{1j}(\tau)}B_{1j}d\tau\\ &+\left(\prod_{i\neq 1,2}^{N} e^{A_{(N-i+1)j}(\tau)}\right)\int_0^{t_2} e^{A_{2j}(\tau)}B_{2j}d\tau+\cdots\\ &+\int_0^{t_N} e^{A_{Nj}(\tau)}B_{Nj}d\tau.\end{aligned} \tag{A2}$$

In (A1) and (A2), $x\ = (i_\alpha\ v_\alpha\ i_\beta\ v_\beta\ v_{C1}\ v_{C2})^{\mathrm{T}}$, which represents, respectively, the $\alpha\beta$ components of the measured output inductor currents ($\vec{i}_{abc}$) and capacitor voltages ($\vec{v}_{abc}$), and the split-capacitor voltages ($v_{C1},\ v_{C2}$). The nonzero elements of the matrix A_{ij}, of dimension 6 × 6, are given by the following:

$$\begin{aligned}A_{ij}(1,1) &= A_{ij}(3,1) = -r_L L_f^{(-1)}, A_{ij}(1,2) = A_{ij}(3,2)\\ &= -L_f^{(-1)}, A_{ij}(1,5) = A_{ij},(1,6)\\ &= 0.5\, L_f^{(-1)}(i\cdot(-1)^{\lceil j/3\rceil})))(2,1)\\ &= -C_f^{(-1)}, A_{ij}(3,5) = A_{ij}(3,6)\\ &= 0.5\, L_f^{(-1)}(i\cdot(-1)^{(j+1)})\\ A_{ij}(4,1) &= A_{ij}(4,3) = A_{ij}(4,5)\\ &= C_1^{(-1)}\frac{1+(-1)^{\lceil j/3\rceil}}{2}(-1)^{(i+1)}, A_{ij}(5,1)\\ &= A_{ij}(5,3) = A_{ij}(5,5)\\ &= C_2^{(-1)}\frac{1-(-1)^{(j+1)}}{2}\end{aligned}$$

where $^{\lceil j/3\rceil}$ represents the ceiling of the ratio. The nonzero elements of the matrix B_{ij}, of dimension 6 × 2, are given by the following: $B_{ij}\ (51) = B_{ij}\ \ (61) = C_1^{-1}\ , B_{ij}\ (22) = B_{ij}\ \ (24) = C_f^{-1}$. In addition to (7b), the following additional equations are needed to solve the model:

$$\vec{i}_{\text{out }\alpha,\beta_k} = T_s\ L_f^{-1}\cdot\vec{v}_{\alpha,\beta_{k-1}} + \left(1 - RT_s L_f^{-1}\right)\vec{i}_{\text{out }\alpha,\beta_{k-1}} \tag{A3}$$

$$v_{NP\,k+1} = v_{C1\,k+1} - v_{C2\,k+1} \tag{A4}$$

where $\vec{i}_{\text{out }\alpha,\beta_k}$ are an estimate of the load currents in the α andβ frames, $v_{NP\,k+1}$ is an estimation of the neutral-point voltage of the inverter, and R is the load resistance.

ACKNOWLEDGMENT

The authors would like to thank Drs. Alan Mantooth and Chris Farnell at the University of Arkansas for their help with the DSP controller hardware.

REFERENCES

[1] J. Selvaraj, “Intentional electromagnetic interference attack on sensors and actuators,” Ph.D. dissertation, Dept. Elect. Eng., Iowa State Univ., Ames, IA, USA, 2018. [Online]. Available: https://lib.dr.iastate.edu/etd/16460

[2] Y. Zhang and K. Rasmussen, “Detection of electromagnetic interference attacks on sensor systems,” in *Proc. IEEE Symp. Secur. Privacy*, 2020, pp. 203–216, doi: 10.1109/SP40000.2020.00001.

[3] Y. Shoukry, P. Martin, P. Tabuada, and M. Srivastava, “Non-invasive spoofing attacks for anti-lock braking systems,” in *Proc. Int. Conf. Cryptogr. Hardware Embedded Syst.*, 2013, pp. 55–72.

[4] A. Barua and M. A. Al Faruque, “Special session: Noninvasive sensor-spoofing attacks on embedded and cyber-physical systems,” in *Proc. IEEE 38th Int. Conf. Comput. Des.*, 2020, pp. 45–48, doi: 10.1109/ICCD50377.2020.00024.

[5] J. Selvaraj, G. Dayanıklı, N. Gaunkar, D. Ware, R. Gerdes, and M. Mina, “Electromagnetic induction attacks against embedded systems,” in *Proc. Asia Conf. Comput. Commun. Secur.*, 2018, pp. 499–510.

[6] O. Aiello, “Hall-effect current sensors susceptibility to EMI: Experimental study,” *Electron. (Basel)*, vol. 8, no. 11, Nov. 2019, Art. no. 1310. [Online]. Available: https://search.proquest.com/docview/2548407225

[7] K. Rayane, H. Abu-Rub, M. Shadmand, S. Bayhan, and A. Benalia, “Grid interactive smart inverter with intrusion detection capability,” in *Proc. IEEE 12th Int. Symp. Power Electron. Distrib. Gener. Syst.*, 2021, pp. 1–6, doi: 10.1109/PEDG51384.2021.9494265.

[8] T. Ding *et al.*, “Quantifying cyber attacks on industrial MMC-HVDC control system using structured pseudospectrum,” *IEEE Trans. Power Electron.*, vol. 36, no. 5, pp. 4915–4920, May 2021, doi: 10.1109/TPEL.2020.3032883.

[9] Y. Tu, V. S. Tida, Z. Pan, and X. Hei, “Transduction shield: A low-complexity method to detect and correct the effects of EMI injection attacks on sensors,” in *Proc. ACM Asia Conf. Comput. Commun. Secur.*, vol. 15, 2021, pp. 901–915.

[10] Y. Shen, L. Wang, J. P. Lau, and Z. Liu, “A robust control architecture for mitigating sensor and actuator attacks on PV converter,” in *Proc. IEEE PES GTD Grand Int. Conf. Expo. Asia*, 2019, pp. 970–975, doi: 10.1109/GTDAsia.2019.8716017.

[11] C. Burgos-Mellado *et al.*, “Cyber-attacks in modular multilevel converters,” *IEEE Trans. Power Electron.*, vol. 37, no. 7, pp. 8488–8501, Jul. 2022, doi: 10.1109/TPEL.2022.3147466.

[12] J. Ramos-Ruiz *et al.*, “An active detection scheme for cyber attacks on grid-tied PV systems,” in *Proc. IEEE CyberPELS*, 2020, pp. 1–6, doi: 10.1109/CyberPELS49534.2020.9311539.

[13] D. F. Kune *et al.*, “Ghost talk: Mitigating EMI signal injection attacks against analog sensors,” in *Proc. IEEE Symp. Secur. Privacy*, 2013, pp. 145–159, doi: 10.1109/SP.2013.20.

[14] A. Sargolzaei, K. Yazdani, A. Abbaspour, C. D. Crane, III, and W. E. Dixon, “Detection and mitigation of false data injection attacks in networked control systems,” *IEEE Trans. Ind. Inform.*, vol. 16, no. 6, pp. 4281–4292, Jun. 2020, doi: 10.1109/TII.2019.2952067.

[15] R. E. Kalman, “A new approach to linear filtering and prediction problems,” *J. Basic Eng.*, vol. 82, no. 1, pp. 35–45, 1960.

[16] A. Laszka, W. Abbas, S. S. Sastry, Y. Vorobeychik, and X. Koutsoukos, “Optimal thresholds for intrusion detection systems,” in *Proc. 3rd Annu. Symp. Bootcamp Sci. Secur.*, 2016, pp. 72–81.

[17] A. N. Shiryaev, “On optimum methods in quickest detection problems,” *Theory Probability Appl.*, vol. 8, pp. 22–46, 1963.

[18] G. Verdier, N. Hilgert, and J.-P. Vila, “Adaptive threshold computation for cusumtype procedures in change detection and isolation problems,” *Comput. Statist. Data Anal.*, vol. 52, no. 9, pp. 4161–4174, 2008.

[19] Z. Feng, X. Zhang, S. Yu, and J. Zhuang, “Comparative study of 2SiC&4Si hybrid configuration schemes in ANPC inverter,” *IEEE Access*, vol. 8, pp. 33 934–33 943, 2020, doi: 10.1109/ACCESS.2020.2974554.